ABSTRACT

Title of Document:	CHARACTERIZATION OF THE INITIAL SPRAY FROM A JET IN CROSSFLOW
	Yinghui Zheng, Master of Science, 2009
Directed By:	André Marshall, Associate Professor, Department of Fire Protection Engineering

An experimental study on the initial spray from a liquid jet in air crossflow was conducted using Shadowgraphy and Particle Image Velocimetry (PIV) techniques. Momentum ratio and gas Weber number were varied to study their effects on the column trajectory, spray trajectory, breakup locations and spray characteristics after column breakup. Correlations for column trajectory, spray trajectory, breakup locations in terms of momentum ratio and gas Weber number were obtained using linear regression of the experimental data. Two breakup modes were recognized in the test (Column breakup and Bag breakup), a breakup mode regime map was provided including effects of momentum ratio and gas Weber number. Drop characteristics in the spray were also investigated.

CHARACTERIZATION OF THE INITIAL SPRAY FROM A JET IN CROSSFLOW

By

Yinghui Zheng

Thesis submitted to the Faculty of the Graduate School of the
University of Maryland, College Park, in partial fulfillment
of the requirements for the degree of
Master of Science
2009

Advisory Committee:
Professor André Marshall, Chair
Professor James G. Quintiere
Professor Arnaud Trouvé

Acknowledgements

This work is funded by the National Science Foundation and I would like to thank their support for this project. I would like to thank my advisor, Dr. André Marshall, for all the precious guidance, patience and support. I learned a lot from you not only about the study and research but also the way to think for my life, which I appreciate very much.

I would like to thank Dr. James G. Quintiere and Dr. Arnaud Trouvé for being my Committee members and all the help and support. I am also grateful for the help that Dr. Xinan Liu gave to me during my experiment, and also thank Dr. Kenneth Kiger for letting me share the experiment facility. Many thanks to Ning Ren for helping me with my research, Brian Salyers for spending countless hours with me on this project, Haiwen Ding for continuously cheering me up for new life.

Last but not least, I'd like to thank my parents and my boyfriend Dongquan Shen, I would not be me without your love and support.

Table of Contents

Acknowledgements ii
Table of Contents iii
List of Figures iv
Nomenclature vi
1. Introduction 1
1.1 Motivation 1
1.2 Literature review 1
1.2.1 JICF Trajectory 1
1.2.2 BU Modes and BU Locations 4
1.2.3 Spray Characterization 6
1.3 Research Objectives 8
2. Experimental Setup and Test matrix 9
3. Results and analysis 13
3.1 Air velocity field characterization 13
3.2 Jet Visualization 15
3.2.1 Initial Liquid flow characterization 15
3.2.2 Column and Bag BU 17
3.3 Liquid/Gas interaction 18
3.3.1 Trajectories of the liquid column 19
3.3.2 Column breakup locations 21
3.3.2.1 BU location in streamwise direction 22
3.3.2.2 BU location in cross-stream direction 24
3.3.3 BU modes and regimes 25
3.3.3.1 Effect of We_G 25
3.3.3.2 Effect of Momentum ratio 26
3.3.3.3 BU regimes map 28
3.3.4 Spray Behavior 30
3.3.4.1 Spray trajectory 30
3.3.4.2 Effects of momentum ratio and We_G on drop size 33
3.3.4.3 Drop size distribution along spray trajectory 34
3.3.4.4 Mass flux along spray trajectory 36
3.3.4.5 Drop velocity distribution 40
4. Conclusion 43
References 46

List of Figures

Fig. 1: Sketch of a typical liquid breakup process in an air crossflow [1]…….....5

Fig. 2: Schematic diagram of the experimental setup……..…..9

Fig. 3: Crossflow velocity field in the test section ranging from 8.3 m/s to 20 m/s....14

Fig. 4: Velocity profile at x = 0 in the test section.....15

Fig. 5: Initial liquid jet visualization.....16

Fig. 6: Visualization of two breakup modes.....18

Fig. 7: Effect of $\bar{q}$ and We_G on column trajectory.....19

Fig. 8: Column trajectory correlation.....20

Fig. 9: Breakup probability histogram, We_G = 6, $\bar{q}$ = 10.....22

Fig. 10: Column breakup location in streamwise direction.....23

Fig. 11: Column breakup location in cross-stream direction.....24

Fig. 12: Breakup mode change with Weber number ($\bar{q}$ = 50, We_G = 4, 8, 16).....26

Fig. 13: Breakup mode change with momentum ratio.....28

Fig. 14: Breakup regimes respecting to We_G and $\bar{q}$ 29

Fig. 15： Trajectory of the spray after jet breakup.....31

Fig. 16: Spray trajectory correlation.....33

Fig. 17: Effect of We_G and $\bar{q}$ on the drop diameter size of the spray.....34

Fig. 18: Drop size distribution along the spray trajectory.....35

Fig. 19: Drop size distribution and mass flux percentage of the spray respecting to streamwise direction.....36

Fig. 20: Histogram of the spray, VF/CVF, NF/CNF.....38

Fig. 21: Dimensionless drop velocity of the spray 41

Fig. 22: Dimensionless drop velocity angle of the spray.....42

Nomenclature

d Jet diameter, mm

d_{diff} Diffraction limited image diameter, mm

d_p Physical diameter of a particle, mm

D Drop diameter, mm

D_{v50} Characteristic drop diameter, mm

$f_{\#}$ F number of the lens

F Wind tunnel frequency, HZ

M Magnification of the optical system

Oh Ohnesorge number, $Oh = \frac{\mu_l}{\sqrt{\rho_l \sigma_l d}}$

$\overline{q}$ Momentume ratio, $\overline{q} = \frac{\rho_l V_j^2}{\rho_a V_a^2}$

Re_G Gas Reynolds number, $\mathrm{Re}_G = \frac{\rho_a V_a d}{\mu_a}$

Re_j Jet Reynolds number, $\mathrm{Re}_j = \frac{\rho_l V_j d}{\mu_l}$

SMD/D_{32} Sauter Mean Diameter, $D_{32} = \frac{\sum_i d_i^3}{\sum_i d_i^2}$

$\overline{V}$ Dimensionless velocity, m/s

u_a Air velocity in *x*-direction, m/s

u_d Droplet velocity in *x*-direction, m/s

u_j Jet velocity in *x*-direction, u_j = 0 m/s

V_a Air velocity magnitude, m/s

V_d Drop velocity magnitude, m/s

V_j Jet velocity magnitude, m/s

V_r Relative velocity, m/s

v_a Air velocity in *y*-direction, v_a = 0 m/s

v_d Droplet velocity in *y*-direction, m/s

v_j Jet velocity in *y*-direction, m/s

w Width of the grid cell, mm

W Width of the spray, mm

We_{cri} Critical Weber number

We_d Droplet Weber number, $\mathrm{We}_d = \dfrac{\rho_l D\left[(u_a - u_d)^2 + (v_a - v_d)^2\right]}{\sigma_l}$

We_G Gas Weber number, $\mathrm{We}_G = \dfrac{\rho_a d V_a^2}{\sigma_l}$

We_j Jet Weber number, $\mathrm{We}_j = \dfrac{\rho_l d V_l^2}{\sigma_l}$

x_b Column breakup location in *x* direction

y_b Column breakup location in *y* direction

Greek letters

ρ_a Air density

ρ_l Liquid density

σ Surface tension

$\bar{\theta}$ Dimensionless velocity angle, $\bar{\theta} = \frac{\theta_d - \theta_j}{\theta_a - \theta_j}$

θ_a Air velocity angle

θ_d Droplet velocity angle

θ_j Jet initial velocity angle

λ Wavelength, um

Subscript

a Air properties

b Column breakup

c Column region

cri Critical value

d Droplet

G Gas phase properties

j Liquid jet

l Liuqid properties

r Relative

s Spray region

1. Introduction

1.1 Motivation

The characteristics of a liquid jet injected transversely into a gaseous crossflow have been studied in the past both experimentally and numerically. The jet in crossflow (JICF) configuration has a board range of applications including air breathing propulsion systems, fire suppression system, and agricultural sprays. In these applications, liquid jets are often injected into a crossflow air current which facilitates the jet breakup, atomization, and dispersion processes that govern the performance of these systems. For example, in combustion systems, the fuel jet spray characteristics determine combustion stability, efficiency, and emissions. While in mobile fire suppression systems (i.e. fire hose streams), the trajectory of the jet and spray characteristics govern fire extinguishing performance. A full understanding of jet breakup mechanisms and the resulting spray will help to make these systems more effective and reliable. Detailed measurements and understanding of jet breakup mechanisms are also required to support advances in spray atomization models for computational analysis of spray systems.

1.2 Literature review

Many researchers have devoted their efforts to study of jet in crossflow characteristics. In these studies, the liquid jet is usually injected perpendicular to the gas crossflow causing bending of the liquid jet and subsequent breakup. In this paper, the literature review will be focused on jet trajectory, jet breakup modes and regimes and spray characteristics.

1.2.1 JICF Trajectory

Jet trajectory is an important characteristic of jets in crossflow which has been widely studied using several approaches. Chen et al. were among those early researchers who studied the structure of the jet using the Mie-scattering technique and found that the jet was composed of three zones (liquid core, ligament and droplet regions) [2]. Based on this assumption and trajectory correlations from previous researchers, they proposed a general functional form in term of the momentum ratio ($\bar{q} = \rho_l V_j^2 / \rho_a V_a^2$) and streamwise direction location (x), which could describe the whole trajectory more accurately. Wu et al. investigated the jet trajectory and breakup properties using a pulsed shadowgraphy technique and developed a simplified power law for the column trajectory correlation based on a force analyses which is a function of $\bar{q}^{1/2}$ [1]. They also identified the column fracture locations and found the transverse breakup distance was a function of $\bar{q}^{1/2}$ while the axial breakup distance was a constant. Iyogun et al. extended previous research to a low subsonic crossflow range, emphasizing the trajectory of the upper boundary of the jet using Laser Doppler Velocimetry (LDV), they also compared jet trajectory correlations given by literature and concluded that the correlation they obtained agreed well with previous studies with some discrepancies [3]. Jet characteristics in crossflow at elevated pressure were investigated by Becker and Hassa, and Cavaliere et al. [4-6]. Becker and Hassa concluded correlations for column trajectory including the effect of momentum ratio based on Mie-scattering measurements. Stenzler et al. studied effect of We_G and viscosity ratio on the trajectory by varying velocity and temperature and proposed two correlations for heated and unheated cases, which were functions of momentum ratio, We_G and viscosity ratio [6]. They also found that We_G and viscosity ratio significantly improved the accuracy of the regression fit over a wide range of

operating condition. Ragucci et al. investigated the effect of Re_G on the cross-stream breakup location and We_G on the streamwise breakup location [7]. Ragucci et al. improved Bellofiore et al.'s work, they studied trajectory and momentum coherence breakdown of jets in crossflow [8]. They first found correlations for the column breakup locations which were then used to normalize measured trajectory and resulted in a simple power law correlation for the trajectory. Momentum ratio $\bar{q}$ and We_G were included in

Table 1. Trajectory correlations from literature.

Correlations	We_G	$\bar{q}$	Reference
$y/d = 1.37\sqrt{\bar{q}(x/d)}$	57-1179	3.4-185	Wu et al. [1]
$y/d = 9.91\bar{q}^{0.44}[1-\exp(-x/d/13.1)]\cdot$ $[1+1.67\exp(-x/d/4.77)]\cdot[1+1.06\exp(-x/d/0.86)]$	N/A	N/A	Chen et al.[2]
$y/d = 1.997\left(\bar{q}(x/d)\right)^{0.444}$	9.3-159	8.3-726	Iyogun [3]
$y/d = 1.48\bar{q}^{0.42}\ln(1+3.56\frac{x}{d})$	90-2120	1-40	Becker and hassa [4]
All test: $y/d = 3.354\bar{q}^{0.442}(x/d)^{0.391}We_G^{-0.088}(\frac{\mu_l}{\mu_{water}})^{-0.027}$ Heated: $y/d = 3.688\bar{q}^{0.430}(x/d)^{0.384}We_G^{-0.110}(\frac{\mu_l}{\mu_{water}})^{-0.108}$	1.3-106.2	18-36	Stenzler et al. [6]
$y/d = 0.909\bar{q}^{0.476}We_G^{-0.128}\,\mathrm{Re}_G^{0.135}(x/d)^{0.35}$	10-500	5-80	Bellofiore[7]

the column breakup correlations. All the trajectory correlations from the literature are either in power-law, exponential or logarithmic forms as shown in Table 1, which might include effects of momentum ratio, We_G, Re_G or viscosity ratio within different value ranges.

1.2.2 BU Modes and BU Locations

The breakup processes of liquid jets injected into subsonic gaseous crossflows were well described in Wu et al.'s paper, as shown in Fig.1 [1]. After the liquid is injected to the crossflow, it will be exposed to aerodynamic forces (drag force) and capillary forces, which affect the breakup process in different ways. The jet may first undergo surface breakup with droplets stripped from liquid surfaces while surface waves grow, then the liquid column may be fattened and deformed into bags, ligaments, and drops. Wu et al. summarized jet breakup characteristics and obtained a breakup regime map in terms of $\bar{q}$ and We_G which showed four breakup regimes as enhanced capillary breakup (We_G < 10), bag breakup (10 < We_G < 40), multimode breakup (40 < We_G < 80) and shear breakup (We_G > 80). Momentum ratio $\bar{q}$ was used to determine whether the liquid jet undergoes column breakup with ($\bar{q}$ is large) or without ($\bar{q}$ is small) surface mass stripping. They also found that the vertical dimensionless breakup distance is a function of $\bar{q}$ while horizontal dimensionless breakup distance is constant, which are shown in Table 2.

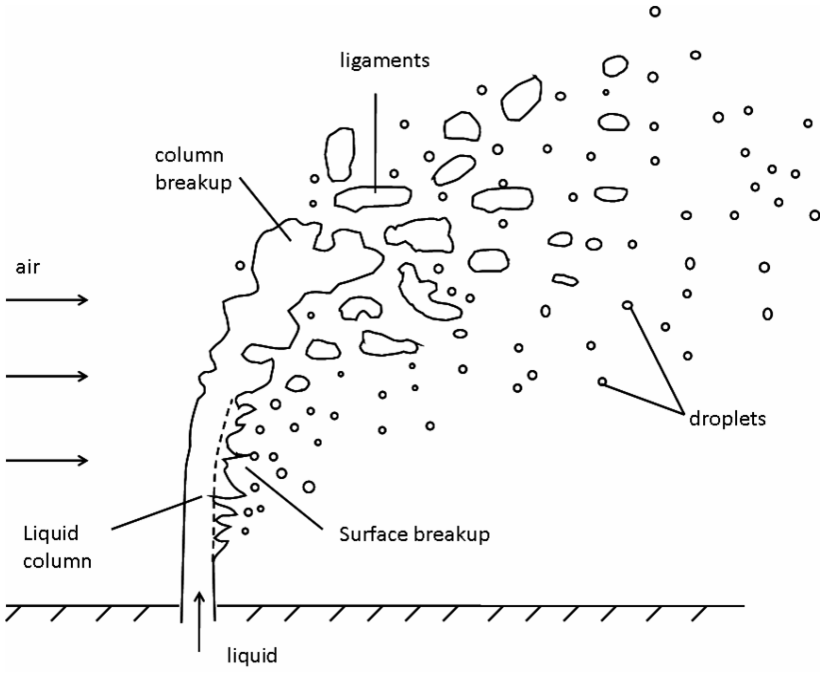

Fig. 1: Sketch of a typical liquid breakup process in an air crossflow [1]

Vich and Ledoux investigated the disintegration of jets in crossflow and concluded that jet breakup regimes were mainly affected by We_G and the shape of the jet was determined by $\overline{q}$ [9]. Their breakup regime map composed of three breakup types as Type I (almost no effect of airflow), Type II as arcade breakup and Type III as bag breakup. Mazallon et al. extended their work on the BU mode regimes study and conclude that there existed four BU regimes which were: Column breakup ($We_G < 5$), Bag breakup ($5 < We_G < 60$), Shear/Bag breakup ($60 < We_G < 110$) and Shear breakup ($We_G > 110$) [10]. They also proposed that primary breakup of a jet in crossflow was similar to secondary BU in drops. Sallam et al. made modification to the BU regimes as: column breakup ($We_G < 4$), Bag BU ($4 < We_G < 30$), Multimode BU ($30 < We_G < 110$) and shear BU ($We_G > 110$) [11]. Primary breakup of a jet in crossflow was also studied by Birouk et al., they found a transition region between arcade type-jet breakup and bag breakup and provided a breakup regimes map based on jet Weber number gas Weber number [12-13]. They also

proposed BU location correlations based on momentum ratio and the Oh ($Oh = \frac{\mu_l}{\sqrt{\rho_l \sigma_l d}}$) number for different liquid viscosity [12].

Recently, Pulat et al. developed a PIV methodology to track the crossflow and characterized the breakup regimes based on We_G [14]. To track the crossflow and reduce reflection from water jet, they seeded the airflow using an atomized mixture (water and a fluorescent powder), which is visible to the CCD camera through an optical filter when excited by laser light.

Table 2. Breakup location correlations from literature.

Correlations	We_G	$\bar{q}$	Reference
$y_b / d = 3.44\sqrt{\bar{q}}$ $x_b / d = 8.06$	57-1179	3.4-185	Wu et al.[1]
$x_b / d = 3.794 We_G^{0.366}$ $y_b / d = 1.449 \bar{q}^{0.476}\ \mathrm{Re}_G^{0.135}$	10-500	5-80	Bellofiore [7]
$x_b / d = \begin{cases} 0.0368q + 14.095\ for \mu_L < 0.019 Pa \cdot s \\ 542.64 q^{0.87} Oh^5\ for \mu_L > 0.019 Pa \cdot s \end{cases}$ $y_b / d = \begin{cases} 3.13 q^{0.53}\ for \mu_L < 0.019 Pa \cdot s \\ 8.60 q^{0.87} Oh^2\ for \mu_L > 0.019 Pa \cdot s \end{cases}$	1.6-13.8	15-284	Birouk et al. [12]

1.2.3 Spray Characterization

After the jet column reaches a certain distance, it disintegrates into bags, ligments and/or droplets. Spray characterization has received as much attention as jet trajectory and jet BU modes by previous researchers. Inamura and Nagai studied the droplet mass flux

distribution, mean droplet size distribution and droplet velocity distribution using a Phase Doppler Particle Analyzer (PDPA) at several downstream locations [15]. They determined a correlation for spray widths as a function of $\bar{q}$ and *x/d*, which was used to calculate the mass flux spatial distribution across the spray based on measured mass fluxes on the centerline. Wu et al. measured spray structures, including droplet size distribution, flux distribution and spray width [16]. They found that large droplets are usually at the top of the spray plume for large $\bar{q}$ conditions while they move closer to the center portion of the plume when $\bar{q}$ is small. What's more, they concluded that spray width was a function of $\bar{q}$ and *x*/d, however, $\bar{q}$ affected penetration much more than spray width. Relying on Pulsed Shadowgraphy and Phase Doppler and Particle Analyzer (PDPA) techniques, Tambe et al. focused on the distribution of droplet sizes and velocities in the spray produced after breakup of the jet [17]. The gas Weber number and $\bar{q}$ were chosen to be the parameters of significance. They obtained similar conclusions as Wu et al.'s, which basically summarized that SMD is dependent upon $\bar{q}$ and gas Weber number. They also found the central portion of the spray plume exhibited a higher uniformity in the droplet distribution. Elshalmy et al. utilized two kinds of techniques (LDV and PIV) to investigate the structure and droplet velocity field of the spray [18]. The PIV technique was proved to be a reliable method to capture the aero-structure of spray generated by liquid jet in detail, and leading, trailing and unsteady vortices were well captured in planar velocity vector field. Recently, Ng et al. experimentally investigated the bag breakup of round non-turbulent liquid jets in crossflow [19], and studied droplets formed in different stages of the jet (from bag membrane, ring and node breakup) which resulted in three distinctive droplets sizes.

1.3 Research Objectives

The present study is aimed at improving understanding of the effects of parameters like momentum ratio and Weber number on the column trajectory, column breakup location and regimes. What's more, the trajectory of the spray needs to be investigated, as discussed in the literature review; more efforts are needed in the characterization of the spray. In the spray region of the jet in crossflow, velocity distribution and drop size distribution needs to be studied in detail. The characteristics of the continuous column and the spray region after column breakup will be discussed in the result in detail.

2. Experimental Setup and Test matrix

A schematic representation of the experimental setup, composed of crossflow system, jet supply system, seeding system and diagnostic system, is shown in Fig. 2. The experiments were conducted in an open circuit wind tunnel, whose test section was composed of four acrylic walls. The liquid jet was injected from the top of the test section, information was recorded by the camera of the Particle Image Velocimetry (PIV) /Shadowgraphy system through transparent walls of the test section. A LaVision seeder was mounted in front of the wind tunnel inlet, where the seeding particle distribution was optimized for air flow velocity measurements using the PIV system.

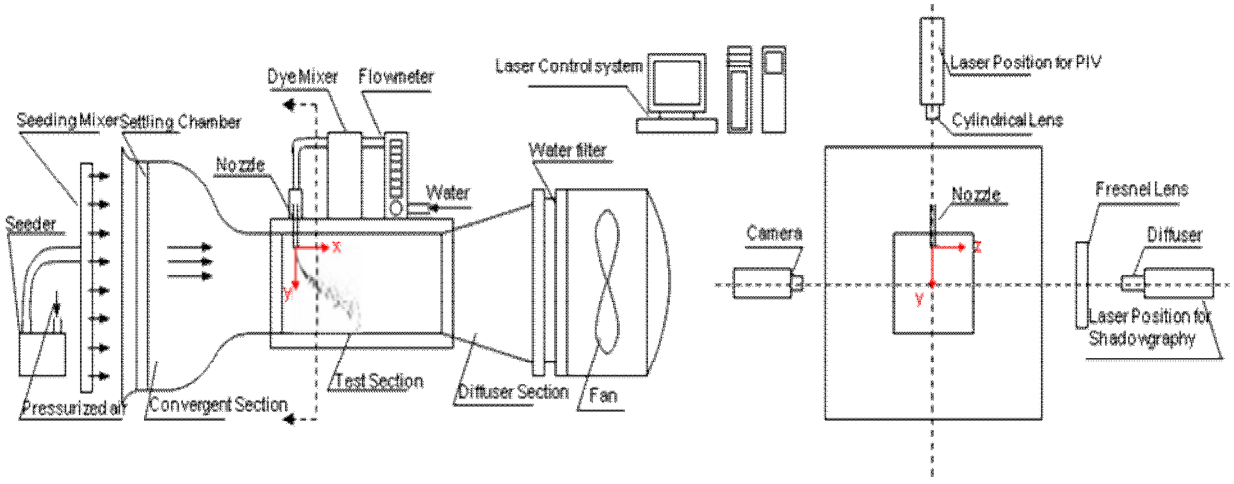

Fig. 2: Schematic diagram of the experimental setup

A commercial wind tunnel from Engineering Laboratory Design was modified for the study. The wind tunnel was composed of a settling chamber, a 3-D convergent section, a test section with dimensions of 300mm x 300mm x 720mm, a diffuser section, a water trap filter layer and a centrifugal fan.

Water was injected into the test section using a stainless steel tube with an inner diameter of 1.1 mm, and the Length / Diameter ratio was larger than 20 to obtain fully developed

turbulent velocity profile [20]. The injection nozzle was mounted in the center of the ceiling and 20 mm away from the inlet of the test section to avoid possible instability.

The test section of the wind tunnel was instrumented with several measurement systems to obtain a comprehensive and detailed characterization of the jet in crossflow problem. A hot wire anemometer was used to measure the velocity at 9 locations in the test section, providing a correlation of the wind velocity based on wind tunnel frequency. The actual air velocity used in the results analysis is from hot wire anemometer measurements. However, the hot wire anemometer could only measure the velocity at a spot, and it might have large error even with a small deviation of the measuring tip. So a LaVision PIV system was used in the experiments, which is a widely used technique for measuring the velocity filed in a plane [21], to provide detailed inlet information and comparison between two measurements.

The system consisted of a Double Pulsed Nd: YAG Laser and a double frame, double exposure CCD camera, Image ProX M4. A beam combining system and frequency doubler were also included in the system, which provided high output energy of green visible light (up to 30 MJ per pulse at 532 nm wavelength). As shown in Fig. 2, laser head with a cylindrical lens was mounted above the test section providing a laser sheet parallel to the *x*-axis. A camera looking perpendicularly from the side of the test section was also used. The laser was pulsed for a very short time (3~5 ns) to illuminate the flow plane, 'freezing' the movement of the particles and creating an image of the intensity distribution of the light scattered from the seeding particles. The pulses were delivered by the laser in pairs separated by about 18 μs. The shutter of the camera was synchronized with the laser to obtain two successive images. Those images were compared by

LaVision post process software, which divided the images into small interrogation windows of a certain size (64 x 64 pixels for this test). The relative position of each interrogation windows between images A and B was shifted until the correlation of the intensity distribution created from the seeding particles was maximized. The spatial shift of the images accorded with the separation time, and provided the local velocity in the interrogation region from dividing it by separation time.

To optimize the measurement results, the image size of a particle should be at least 1 pixel, which is given by [21]:

$$d_i = \sqrt{(Md_p)^2 + d_{diff}^2} \quad (1)$$

Where d_p is the physical diameter of the particle, M is the magnification of the optical system and d_{diff} is the diffraction limited image diameter given by:

$$d_{diff} = 2.44 f_{\#}(M+1)\lambda \quad (2)$$

Where $f_{\#}$ is the *f*-number of the lens system and λ is the wavelength of the incident light on the particle. The field of view (45 mm x 45 mm), *f*-number of the lens were carefully set to make sure the image size of seeding particle is larger than the criterion.

The travel distance of a particle during the time interval between two laser pulses was also calculated using Equ. 1, and the image size of the travel distance was designed to be approximately 8 pixels by adjusting the time interval.

The velocity field in the region of liquid jet was measured, and 300 images were taken for each case, average velocity information was exported from the DaVis post process software and plotted using Tecplot.

The Shadowgraphy technique was used to capture the liquid jet information, whose setup was slightly different from the one in the PIV measurement. As shown in Fig. 2, the

camera was still in the same location (distance from the test section was modified due to the change of the field of view), while the laser head was mounted at the other side, aligned with the laser head. In this setup, the cylindrical lens was replaced by a diffuser to provide a uniform light background. A Fresnel lens was mounted between leaser head and test section to expand the laser light background to cover a larger field of view. The shutter of the camera opens twice with a small separation time (around 100 ms) and creates two successive images of the light intensity distribution of the shadow of the drops in the field of view. The drop sizes are determined using an edge detection algorithm provided by the LaVision Sizing Master software. A Particle Tracking Velocimetry (PTV) algorithm also included in the software uses the shadowgraph image pairs to track the shift between adjacent similarly sized particles. The displacement determined from the calibrated images along with the separation time provides velocity information for every drop.

The images for each case were exported from the DaVis post process software and column trajectory, breakup locations were collected from those images. Droplets information including drop locations, velocity and sizes were given by DaVis post process software, however, even with optimized configuration for the software, there were still some droplets with unrealistic velocities (for example negative values). So a Fortran code was used to get ride of those wrong information and histogram of the whole jet spray.

3. Results and analysis

For the Hot wire Anemometer measurement, to obtain velocity data from several locations inside the test section, another top with 9 holes was designed for the air velocity measurement. These holes were designed to allow measurements at the upstream, downstream and the liquid jet injection locations.

The experiment was conducted in a lab environment, where the ambient temperature was 20°*C*, the density of the air and water is 1.2 kg/m^3 and 998 kg/m^3 respectively. Viscosity was used to calculate Re_j, which is 1.83e-05 kg/ms and 0.001003 kg/ms for air and water. Surface tension of the water, which is 0.0728 N/m, was used to calculate Weber number.

Injection velocity was varied from 2.9 to 8.0 m/s and the air velocity was limited from 10 to 30 m/s. The water was injected from a nozzle with 1.1 mm in diameter to produce the following conditions: $\bar{q}$ of 10-50, We_G of 4 to 16, We_j of 20 to 800, Re_j of 2000 to 8000 , Re_G of 100 to 2200. These ranges of test conditions covers both column and bag BU regimes.

Results on the initial spray of the jet in crossflow will be discussed in the following sections, in terms of air velocity field, liquid column trajectory, spray trajectory, BU location, BU modes, and spray behavior after jet BU.

3.1 Air velocity field characterization

The air velocity in the test section was characterized using Hot Wire Anemometer and PIV. Results from both methods agree with each other within an acceptable error.

The average velocity range measured by the hot wire anemometer was from 8.3 m/s to 19.2 m/s. As shown in Fig. 3, air velocity in different height of the test section is plotted for three air average velocities. The upper plane is located at the height of the nozzle exit,

which shows the crossflow at injection. The second measurement is in the middle of the test section and the lower plane is approximately symmetric with the upper plane. The velocity variation for both the top plane of the test section and the bottom plane share a similar pattern, which exhibits lower velocity in the upstream corner and diagonally increasing velocity to the downstream corner. All velocities are within 5% of the mean throughout the test section over the full range of the wind tunnel operation conditions. This behavior may be due to the centrifugal fan which produced uneven negative pressure across the test section, while the water filters which were mounted between diffuser section and the fan might also contribute to this variation.

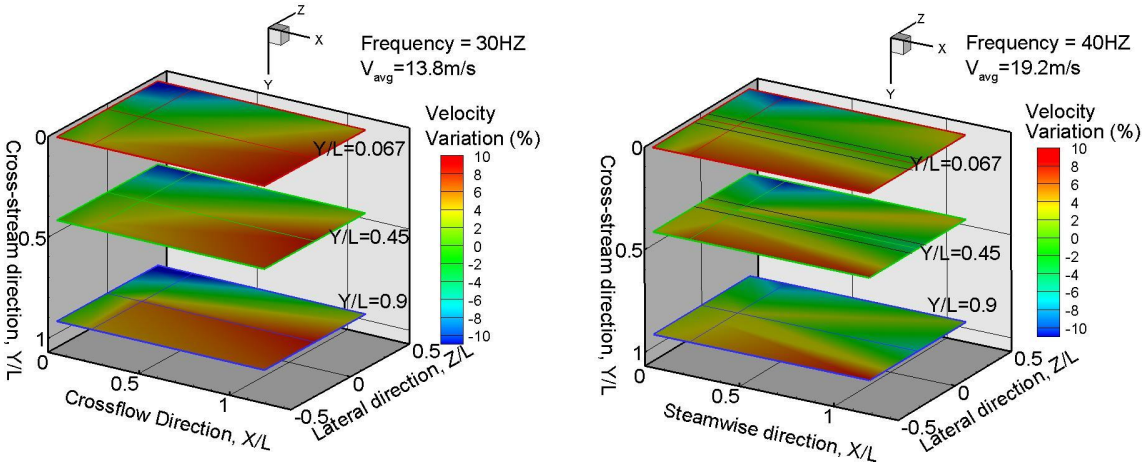

Fig. 3: Crossflow velocity field in the test section ranging from 8.3 m/s to 20 m/s

When the wind tunnel frequency increases to 40 HZ (with average velocity of 19.2 m/s), the velocity variation becomes parallel to the air flow direction with even smaller test section velocity variation around 0 % in the centerline. Considering the jet diameter is 1.1mm and the spray width is less than 5mm, it is reasonable to consider that the liquid jet interacts with a uniform air velocity field.

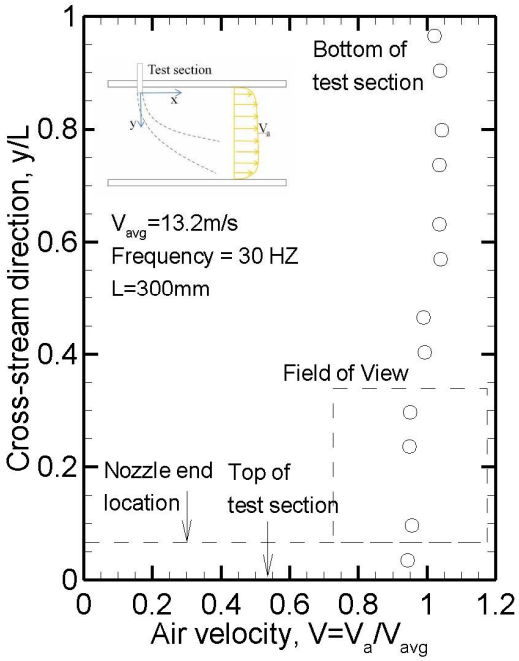

Fig. 4: Velocity profile at $x = 0$ in the test section

Six measurements were conducted to characterize the air velocity profile in y direction at $x = 0$, since the field of view for PIV measurement is 45 mm x 45 mm, while the height of the test section is 300 mm. As shown in Fig. 4, the air velocity profile normalized by the average velocity in the streamwise direction is very uniform. In our field of view, the velocity profile is approximately 97% of the average velocity and varies less than 5% about the mean.

3.2 Jet Visualization

In this study, two different breakup modes of the jet in crossflow were observed during the test, which are column breakup and bag breakup. In this section, the characteristics of these two breakup modes will be discussed and compared descriptively.

3.2.1 Initial Liquid flow characterization

The nozzle has an inner diameter of 1.1 mm and a length/diameter ratio larger than 20 to make sure flow in the nozzle is fully developed [20]. The initial jet diameter at the nozzle exit is estimated to be 1.09 mm from the images. These images also indicate that cavitation does not influence the initial jet. Fig. 5 shows pulse shadowgraphy images of the initial jet in crossflow over a range of conditions.

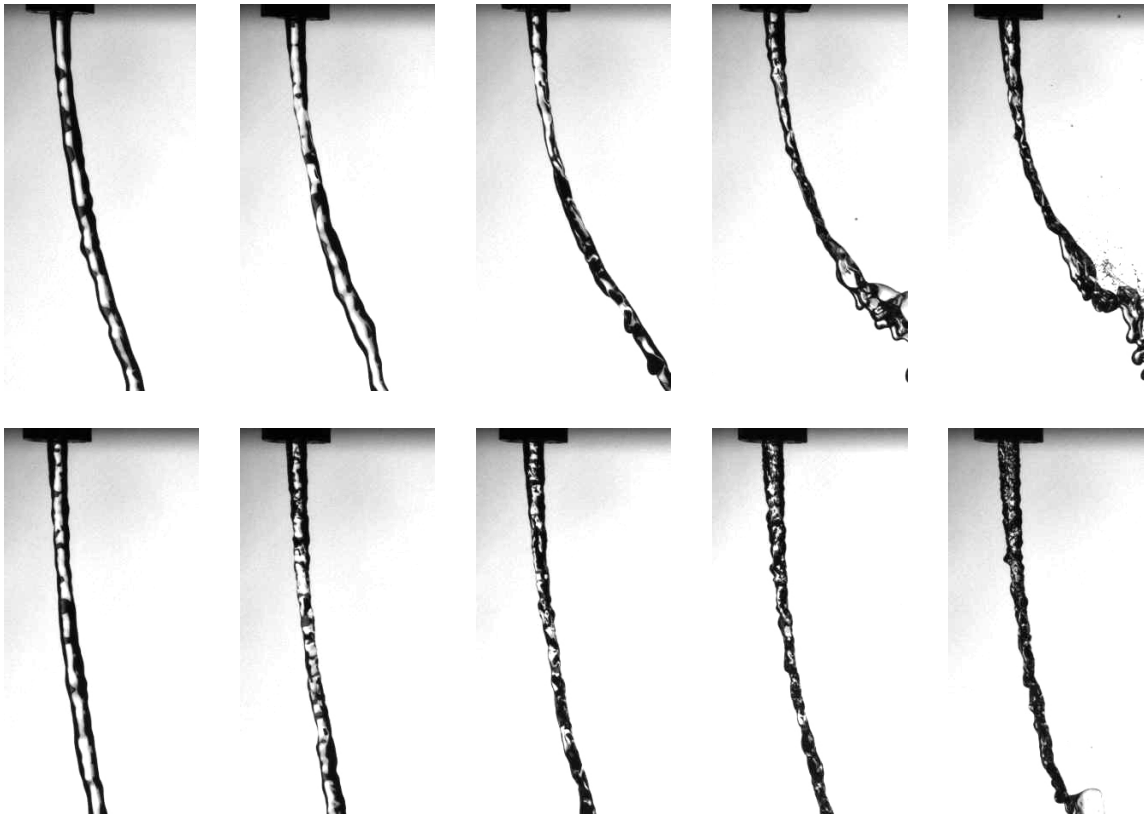

Fig. 5: Initial liquid jet visualization (Top group, $\bar{q}$ = 20, We_G = 4, 6, 8, 12, 16
Bottom group, $\bar{q}$ = 50, We_G = 4, 6, 8, 12, 16)

Results are listed with increasing momentum ratio $\bar{q}$ from top to the bottom group, and increasing We_G from left to right. The wave appeared on the jet were caused both by the turbulence (all of those liquid jets had Re_j > 2000) in the liquid jet and also by the air flow. When $\bar{q}$ and We_G are low, the jet surface is smooth with small disturbances or

protrusions at the beginning of the liquid jet. At a certain distance from the exit, surface wave appears on the jet, whose wavelength decreases with higher $\bar{q}$ and We_G.

3.2.2 Column and Bag BU

As mentioned in previous section, there are four modes of primary breakup of the liquid jets which were characterized by the crossflow Weber number We_G. For present study, two breakup modes were investigated and flow visualization results are illustrated in Fig. 6.

When the air crossflow velocity is low (small We_G), the jet exhibits column breakup mode which is governed by the capillary force since the drag force from the crossflow is comparatively small in this circumstance. The liquid jet undergoes bending in the crossflow direction as seen in Fig. 6. (a), and also deforming from its initial circular shape as indicated by its thinning profile [22]. This deflection of the jet trajectory is from the drag force of the air crossflow as a whole while the deformation of the cross-section of the jet (thinner profile) is due to the uneven pressure distribution with lower pressure at it sides. Thickened regions (nodes) appear along the liquid column and define the wavelengths of column waves. Finally, these waves breakup when the drag force increases and the jet is more 'flat' with increased drag coefficient.

As described in the literature, bag breakup mode appears when air We_G is between 4 and 30 [11]. However in this study, bag breakup mode was not observed until the We_G reached up to 8 as shown in Fig. 6. (b). In this regime, drag forces play the same role to flatten the liquid jet into ellipsoidal shape and deflect the trajectory in the air streamwise direction as it does in column breakup. When the We_G increases to a critical value (We_G = 8), bag-like structures (bags) develop between the nodes [19], which are very much

like the secondary breakup of droplets within bag breakup regime [23]. When the bags grow along the liquid column in the streamwise direction of the crossflow, they expand and become thinner and finally breakup into two crescent-shaped strings (rings) which connect the nodes. Breakup of the strings produces relatively larger droplets than the ones directly from breakup of the bag, while drops formed by the breakup of the remaining nodes are largest [23].

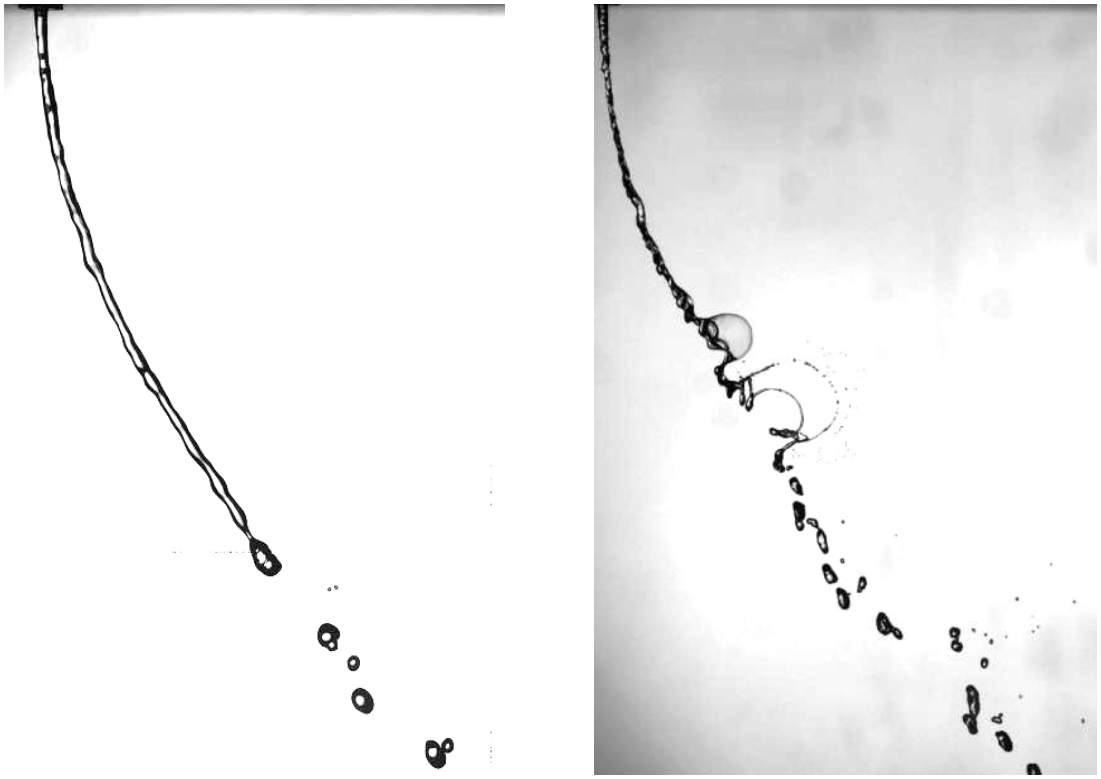

a) Column breakup, We_G = 4, $\bar{q}$ = 20. b) Bag breakup, We_G = 8, $\bar{q}$ = 50

Fig. 6: Visualization of two breakup modes

3.3 Liquid/Gas interaction

After the liquid jet is injected perpendicularly into the air flow, interaction between the liquid and gas phases makes the jet bend in the air flow direction, surface waves on the liquid jet finally breaks up into drops (spray). In this section, we will discuss column

trajectory, column breakup location, regimes and spray behaviors including spray trajectory, drop size and velocity distributions.

3.3.1 Trajectories of the liquid column

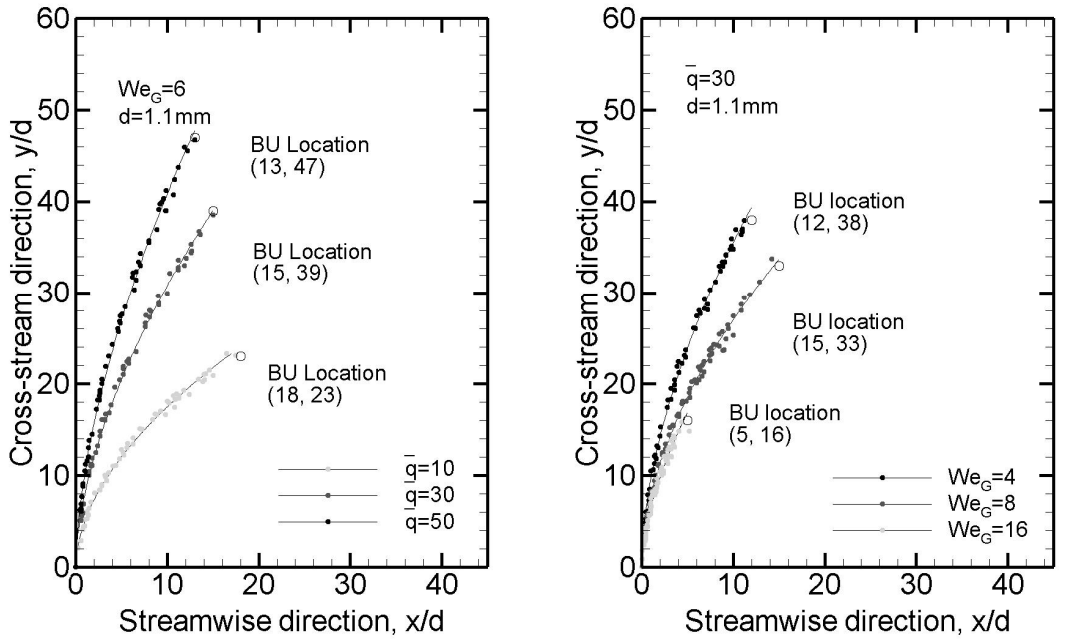

a) Effect of $\bar{q}$ on column trajectories. b) Effect of on column trajectories.

Fig. 7: Effect of $\bar{q}$ and We_G on column trajectory

The results presented in Fig. 7 are the trajectories (normalized by jet diameter) of the upper boundary of the liquid jet column (before the onset of breakup) for varied $\bar{q}$ and We_G respectively. Here the 'upper boundary' is defined in the same way as in Iyogun et al.'s work, which is the windward side of the liquid jet [3].

Fig. 7. a illustrates the effect of $\bar{q}$ on column trajectories with same We_G ($\bar{q}$ = 10, 30, 50), which shows that momentum ratio has a determining effect on the column trajectory shape. Assume column breakup time is dependent on We_G, velocity acceleration in the streamwise direction is determined by drag force since by We_G for the same liquid, and it

also can be concluded that breakup location in the *x* direction is close to a constant with different momentum ratio as shown in Fig. 7. a. Similarly, Fig. 7. b shows the effect of We_G on column trajectories with same momentum ratio $\bar{q}$ (We_G = 4, 8, 16). The gas Weber number was changed by varying the air crossflow velocity, while the liquid jet velocity was also adjusted to keep momentum ratio constant. Under the same momentum ratio conditions, the total length (including both streamwise and cross-stream direction penetration) of the column trajectory decreases sharply with increasing We_G. The column trajectory tends to maintain the shape but breakup earlier with larger Weber number.

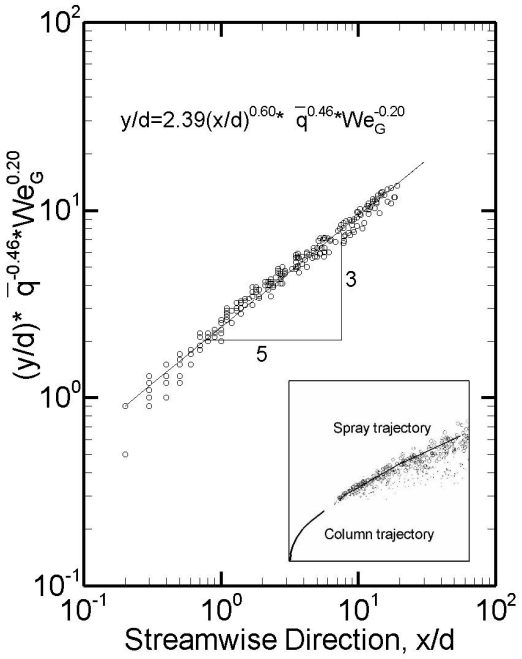

Fig. 8: Column trajectory correlation

A simple linear regression (Ordinary Least Square), which was used by several researchers [1, 3, 16], was used to determine the best fit for the column trajectory, which has the following form:

$$\frac{y}{d} = A\left(\frac{x}{d}\right)^{B} q^{C} We_G^{D} \tag{3}$$

Then the natural logarithm of Eq. 4 is taken, and obtains:

$$\ln(\frac{y}{d}) = \ln(A) + B\ln\left(\frac{x}{d}\right) + C\ln q + D\ln(We_G) \tag{4}$$

From which the constants A, B, C, D can be determined by linear regression using Matlab, which gives:

$$\begin{aligned} &\frac{y_c}{d} = 2.39\left(\frac{x_c}{d}\right)^{0.60} \bar{q}^{0.46} We_G^{-0.20} \\ &0 < \frac{x_c}{d} < 20, \quad 10 < \bar{q} < 50, \quad 4 < We_G < 16 \end{aligned} \tag{5}$$

This correlation predicts the column trajectory with high accuracy, standard errors for the coefficient, power of x_c/d, $\bar{q}$ and We_G are 0.054, 0.006, 0.012 and 0.014 respectively, and each t-statistics value of these factors is larger than 3 indicating that all the coefficients are significant at 1% significant level, which means they are all reliable [24]. R-squared of the regression analysis for the overall test conditions of is 0.98, and root mean square error is 0.10.

Trajectory study in previous works focused on the effect of momentum ratio and paid relatively less attention on We_G [1, 5, 16], however, results from this study show both effect of $\bar{q}$ and We_G on trajectory and breakup locations which will be discussed in detail in the following section.

3.3.2 Column breakup locations

In the experiment, 300 images were taken for each case, the breakup location is determined using a probability analysis method, which considers the location where has

the highest possibility for the column trajectory to breakup using a histogram map of breakup probability.

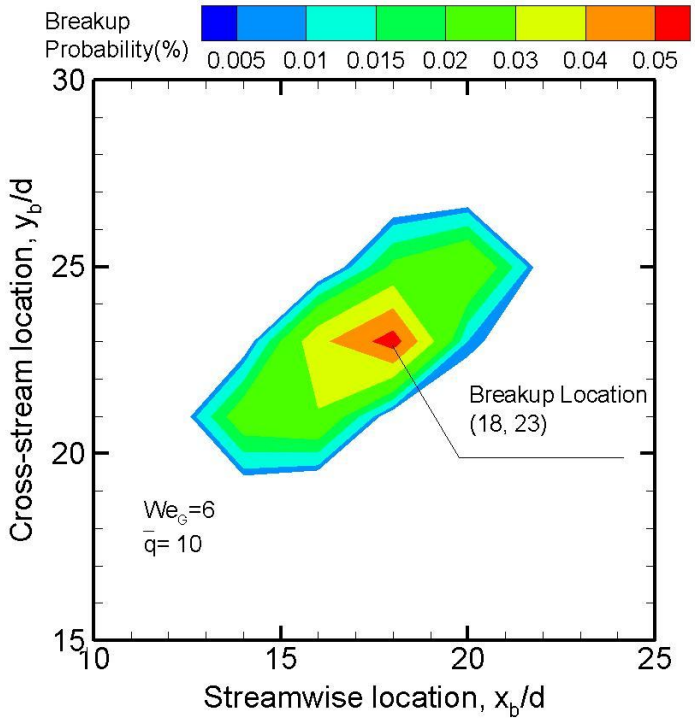

Fig. 9: Breakup probability histogram, We_G = 6, $\bar{q}$ = 10

The breakup probability used in Fig. 9 was calculated by a Matlab code, which divides the interested area into a certain amount of grids and counts how many times liquid jet will breakup in each location (grid), then divides this value by the total number of images and grid area. It can be found that breakup location is in a certain range other than an exactly point even with same $\bar{q}$ and We_G. This fluctuation of the results might come from the wind tunnel whose air velocity filed in the test section is not constant, or the liquid jet velocity is changing over time, or nature of atomization process.

3.3.2.1 BU location in streamwise direction

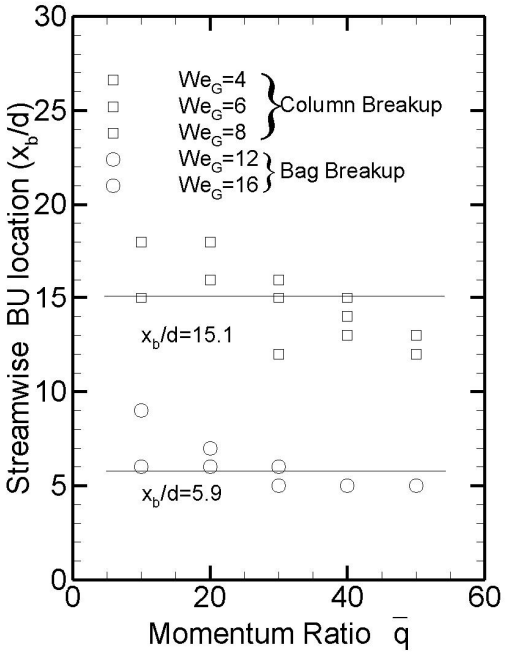

Fig. 10: Column breakup location in streamwise direction

Fig. 10 shows the column breakup location normalized by the jet nozzle diameter against momentum ratio for five different air Weber number conditions in the crossflow streamwise direction. Consistent with the literature, normalized breakup location in *x* direction is considered to be a constant at 8.06 [1], 14.97 [17] or 9.3 [25]. In this study, results show that the streamwise breakup location also decreases with increasing air crossflow velocity hence higher We_G, while change caused by increasing momentum ratio is negligible. From Fig. 10, breakup location can be divided into two regimes respecting to We_G as following:

$$\frac{x_b}{d} = \begin{cases} 5.9 & \text{for } \mathrm{We_G} > 8 \\ 15.1 & \text{for } \mathrm{We_G} \le 8 \end{cases} \tag{6}$$

This formula indicates that the jet tends to breakup early when gas Weber number is larger than a critical value, thus the breakup distance in *x* direction decreases, which agrees with Sallam et al.'s conclusion that column breakup time varies inversely with We_G [11]. However, when We_G is larger than the threshold, *x*-direction BU location finally comes to a constant, which is resulted from decreasing breakup time and increasing jet velocity in streamwise direction result. Due to the limitation of this study, the constant might be different when there are more cases with We_G smaller than 8.

3.3.2.2 BU location in cross-stream direction

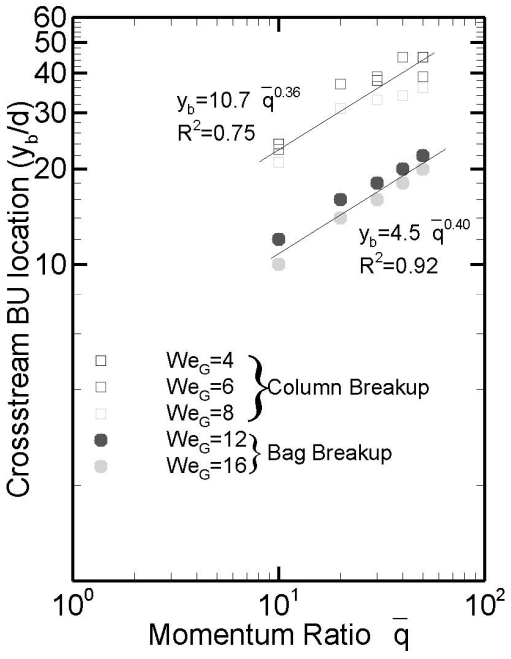

Fig. 11: Column breakup location in cross-stream direction

Similar as column breakup location in streamwise direction, breakup location normalized by nozzle diameter in cross-stream direction is also plotted in Fig. 11. As we can see from the plot, data points collapse into two groups like streamwise direction breakup locations regarding We_G, the best fit found for y_b/d is:

$$\frac{y_b}{d} = \begin{cases} 10.7\bar{q}^{0.40} & \text{for } \mathrm{We_G} \le 8 \\ 4.46\bar{q}^{0.40} & \text{for } \mathrm{We_G} > 8 \end{cases} \tag{7}$$

It could conclude that the effects of momentum ratio on BU locations in cross-stream direction for all cases are in the same order, however, the coefficient decreases sharply when We_G reaches a critical value. This is consistent with Eq. 7 and could be explained by the BU time in [11].

3.3.3 BU modes and regimes

3.3.3.1 Effect of We_G

We_G effect on the breakup of liquid jet column is illustrated in Fig. 11, from which the breakup mode transition can be clearly seen respecting to We_G. We_G was increased by increasing the air crossflow velocity while the liquid jet velocity was also raised to keep the momentum ratio constant. When We_G is small ($We_G < 8$), liquid jet exhibits column breakup mode with ligaments and big droplets after breakup. After We_G increases beyond a critical value ($We_G = 8$ in this study), bag breakup mode appears and there are more drops with different dimensions formed after the breakup.

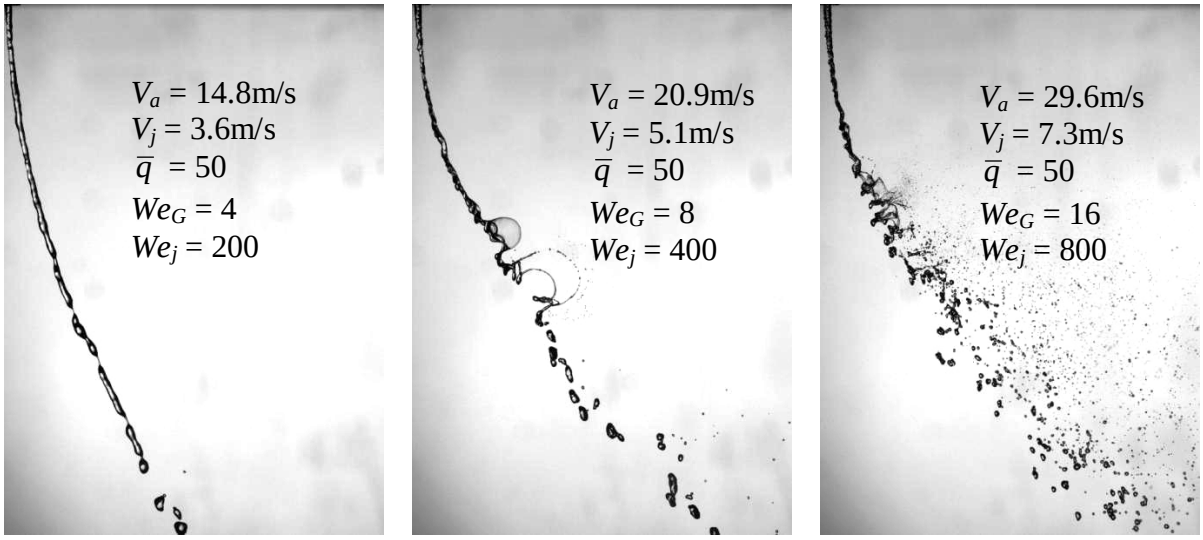

Fig. 12: Breakup mode change with Weber number ($\bar{q}$ = 50, We_G = 4, 8, 16)

The liquid jet bag breakup is similar with droplet bag breakup as studied by Pilch and Erdman, they showed how a liquid drop falling in a counter-ascending air current first deformed, then destabilized and finally broke into stable fragments and droplets [26]. Gas Weber number is used to measure how much drag force is exerted on the liquid column, when drag force reaches a critical value compared to the surface tension force, the bag structure appears after the column breaks and forms smaller drops from bag membrane as well as bigger drops from bag rims.

3.3.3.2 Effect of Momentum ratio

To investigate the effect of momentum ratio on the breakup mode, only the liquid jet velocity was varied for this set of test. Fig. 13 illustrates how liquid jet breakup modes change with different $\bar{q}$ value, and proves that breakup mode is also actually affected by momentum ratio. As we can see from Fig. 13 a, surface waves on the liquid jet develop as the drag force exerts on the jet, the column first breaks up into arcade shape structure or ligaments as described in Vich and Ledoux's work [9], then these structures breakup into smaller drops. In this condition, liquid jet velocity is relatively low compared to air

velocity (V_a = 20.9 m/s, V_j = 2.3 m/s), the liquid body is 'soft' with lower momentum when facing the crossflow which not only breaks the liquid column but also shape the column into arc structures. When the momentum ratio increases by increasing the liquid jet velocity, the jet still exhibits column breakup mode. There are some nodes that appear in the liquid body, those thinner regions between nodes are then stretched and broke up into big droplets with some smaller ones. For the first two cases, they are both in column breakup mode regime. However, with higher momentum ratio, a completely different breakup mechanism (bag breakup mode) is displayed in the last case of Fig. 13. Similar as in previous cases, surface waves on the liquid column develops, nodes and thinner regions appear on the column, and bag structures are formed at the jet breakup location. The bag membrane breaks up into smaller drops, while the nodes form comparatively large droplets.

In this study, we use gas Weber number to differentiate breakup modes consistent with previous research; however, what really decides the breakup mechanism is the relative velocity between liquid column and gas crossflow. Gas velocity and liquid jet velocity both affect the relative velocity hence the breakup mode. Gas Weber number We_G describes how much gas velocity contributes to the breakup, and momentum ratio quantitatively tell us how much jet velocity affects the breakup mode compared to gas velocity. Since the relative velocity between liquid jet and air crossflow is difficult to calculate and compare, gas Weber number and momentum ratio (or jet Weber number We_j) are used together to describe the breakup mode.

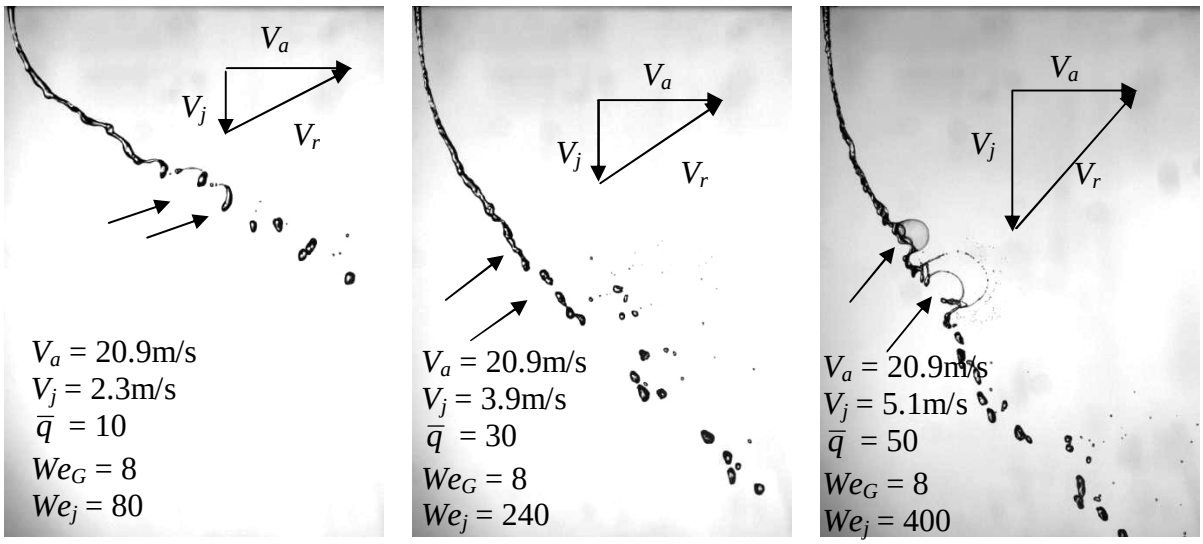

Fig. 13: Breakup mode change with momentum ratio

(We_G = 8, $\bar{q}$ = 10, 30, 50 and We_j = 80, 240, 400)

3.3.3.3 BU regimes map

To identify the jet breakup mode regimes, parameters including air velocity and liquid jet velocity were varied over the test. We_G and momentum ratio were increased gradually from lower value to higher value during the experiment, whose results shows that there is a transition region for the breakup mode change if we use gas Weber number and momentum ratio as the criterion to determine breakup modes. This result agrees with previous study in the literature which proposed four breakup modes and regimes. In the experiment, two different breakup modes were observed, which are column breakup and bag breakup modes, the breakup regime range and transition region was also determined as shown in Fig. 14. As discussed in the previous section, gas Weber number determines the breakup mode, which will change from column breakup mode

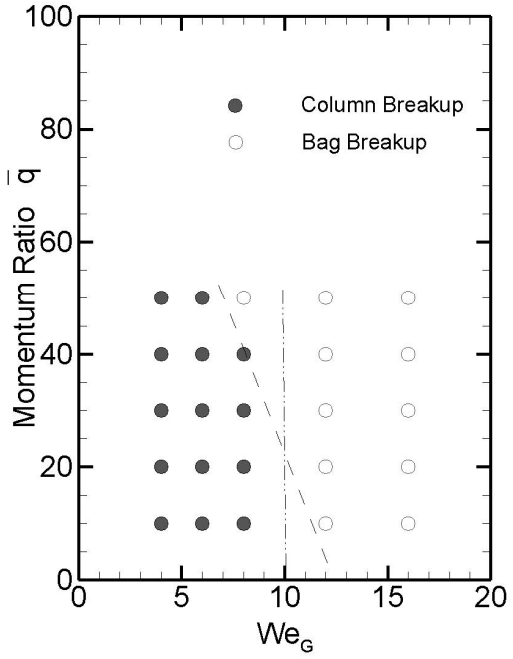

Fig. 14: Breakup regimes respecting to We_G and $\overline{q}$

to bag breakup mode when We_G reaches up to a critical value. However, the effect of momentum ratio on the breakup mode is determined by the gas Weber number: Momentum ratio effects can be neglected in the range $10 < \overline{q} < 50$ when $We_G < 8$; further when $8 < We_G < 12$, increasing momentum ratio could result in BU mode change. This observation is consistent with Sallam and Birouk's work while the critical gas Weber number for the transition is slightly different as listed below：

Table 1: Jet breakup modes and ranges

Regimes	Present work	Reference[11]	Reference[12]
Column Breakup	$We_G < 8$	$We_G < 4$	$1 < We_G < 7$ and $141 < We_j < 315$
Transition	$8 < We_G < 12$	N/A	$3 < We_G < 9$ and $149 < We_j < 939$
Bag Breakup	$12 < We_G$	$4 < We_G < 30$	$4 < We_G < 14$ and $323 < We_j < 1119$

3.3.4 Spray Behavior

The characteristics of the spray formed after the liquid column breaks are of critical interest. In the following sections, the spray trajectory, droplet distribution, droplet size and velocity distributions will be discussed.

3.3.4.1 Spray trajectory

In this paper, spray trajectory is defined as the maximum volume flux line of the spray. At the beginning of the spray, it is shifted lower compared to the column trajectory which is defined as the upper (windward) side of the liquid column (consistent with previous researchers). Fig. 15 shows trajectories (both column and spray trajectory) of the jet under the same We_G but different momentum ratio. There are several steps to obtain the spray trajectory information using volume flux. First, it is important for the calculation of volume flux to determine if the measurement covers the whole lateral depth of the spray. The lateral dispersion of the jet could be estimated using correlation given by Becker and Hassa [4]:

$$\frac{y}{d} = 2.32\bar{q}^{0.09}\left(\frac{x}{d}\right)^{0.32} \quad (8)$$

The maximum streamwise distance (x/d) in our measurement is 100, assuming this formula is still good for momentum of 50, the maximum lateral dispersion is calculated as 13.5mm. The depth of field of the camera for the Shadowgraphy system was around 25mm, which covered the whole lateral depth of the jet with camera focusing on the center of the jet. The whole field of view of measurement (84 mm x 84 mm) was divided into 27 x 27 small cells and the volume flux for each cell was calculated as:

$$\dot{V} = \frac{\sum_i \left(u_d \cdot \frac{1}{6} \pi D^3 \right)_i}{w} \tag{9}$$

Here w is the width of the cell which could be adjusted during the post process.

When the volume flux distribution of the spray was determined, the spray trajectory which connected maximum values of flux could be identified as seen in the Fig. 12.

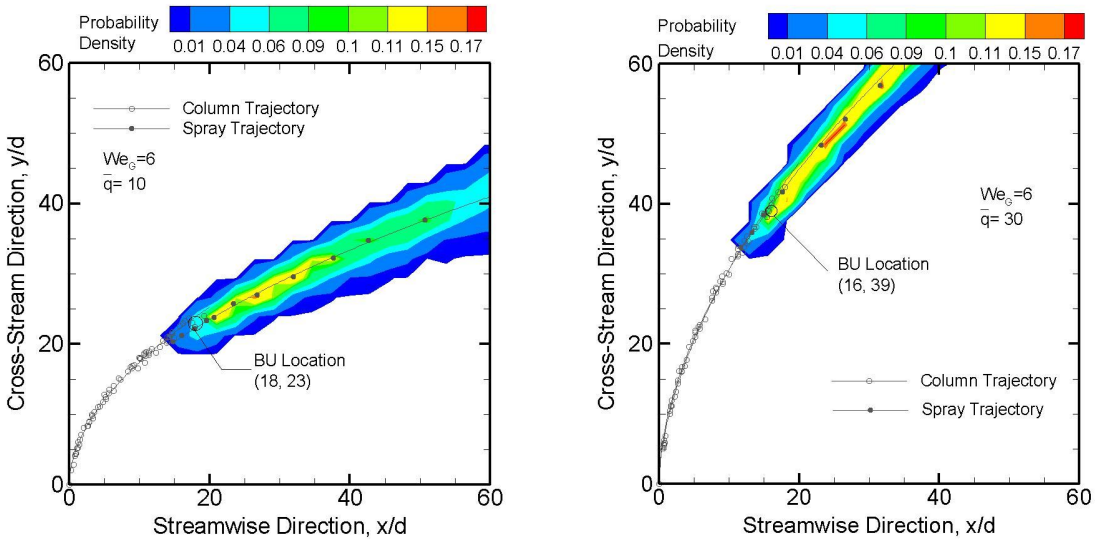

a) We_G = 6, $\bar{q}$ = 10 b) We_G = 6, $\bar{q}$ = 30

Fig. 15: Trajectory of the spray after jet breakup.

When the trajectory for every test condition was obtained using this method, a linear regression method (Ordinary Least Square) was used to correlate the data as we did for the column trajectory, and a formula for the spray trajectory is listed as below:

$$\frac{y_s}{d} = 1.95\left(\frac{x_s}{d}\right)^{0.60} \bar{q}^{0.60} We_G^{-0.38}$$
$$10 < \frac{x_s}{d} < 100, \quad 10 < \bar{q} < 50, \quad 4 < We_G < 16 \tag{10}$$

Spray trajectory data collapse well using this correlation as shown in Fig. 16, with standard error for the power of (x_s/d), $\bar{q}$, and We_G less than 0.01, and the constant's standard error of 0.027. This linear regression is considered to be good with a R-squared of 0.97 and root mean square error of 0.07. This correlation quantitatively describes how much $\bar{q}$ and We_G affect the spray penetration, which increases with higher momentum ratio and decreases with higher gas Weber number. Compare the spray trajectory correlation provided in Eq. 11 with column trajectory correlation provided in Eq. 6, it is apparent that streamwise distance (x/d) contributes same amount to the variation of the penetration of both column and spray trajectory. However, impact of momentum ratio on the spray trajectory is stronger than impact on column trajectory, which is also true for gas Weber number. This is because after the liquid column breaks into drops which form the spray, the surface/volume ratio is increased significantly and the actual drag coefficient is also higher considering shape change (from cylinder column to sphere drops). Hence the drag force effects are fortified after column breakup (represented by increased $\bar{q}$ and increased We_G).

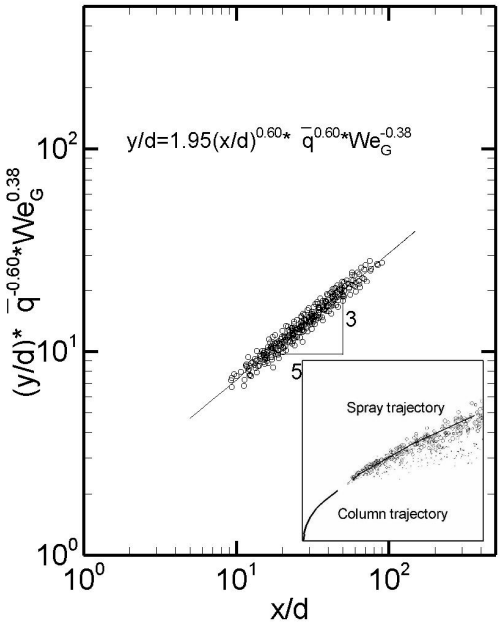

Fig. 16: Spray trajectory correlation

3.3.4.2 Effects of momentum ratio and We_G on drop size

Sauter Mean Diameter (SMD) or D_{32} is defined as the diameter of the sphere that has the same volume/surface area ratio as a particle of interest, as the mean value displayed in a surface area distribution of these particles. The equation for the surface mean is shown as below:

$$D_{32} = \frac{\sum_i d_i^3}{\sum_i d_i^2} \tag{11}$$

D_{v50} is another way to describe the distribution of interested particles, which is the median for a volume distribution of a group of particles.

SMD and D_{v50} of the global spray for all the tests in the experiment are plotted in Fig. 17. Increasing Weber number results in smaller SMD and D_{v50}. it can be predicted that if Weber number increases to a certain big value, SMD and D_{v50} will keep decreasing close

to a small value. We can also see from the plots that when We_G is smaller than 8 or larger than 12, the effect of momentum ratio on SMD and D_{v50} is negligible. When We_G is smaller and the jet is in the column breakup regime, SMD and D_{v50} are both larger than 1.5mm, which is even larger than the jet diameter (1.1mm). After the jet reaches to the bag breakup regime, SMD and D_{v50} decrease close to 0.5 mm, which is around half of the initial jet diameter. There is a transition region between column breakup and bag breakup, the momentum ratio affects drop size when the transition occurs and higher $\overline{q}$ makes transition earlier.

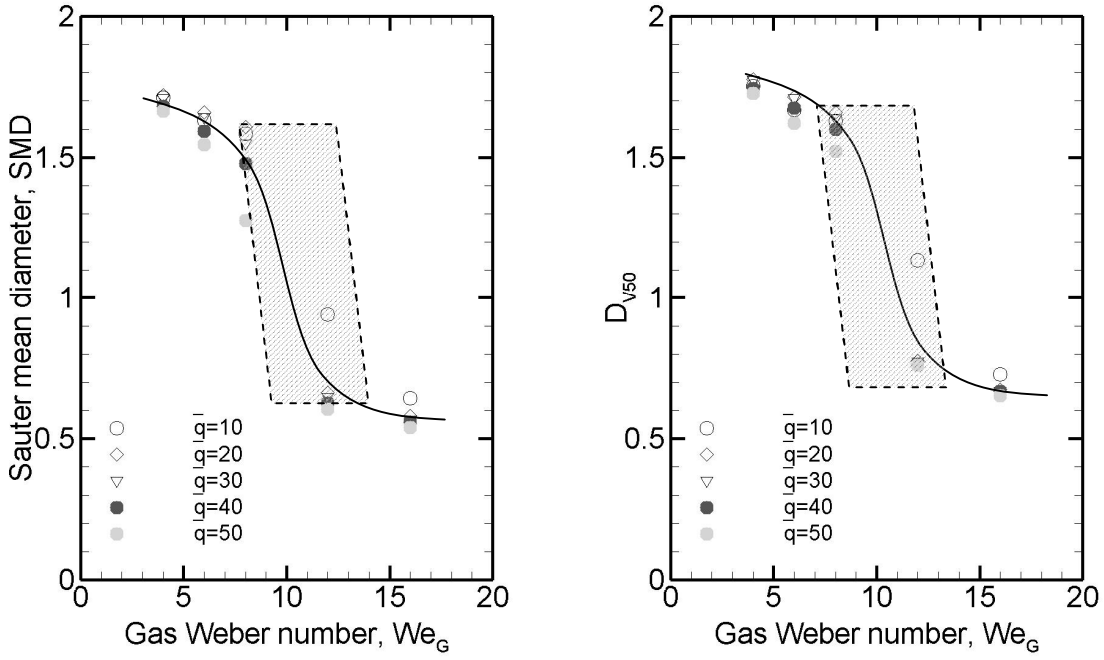

a) SMD of the spray b) D_{v50} of the spray

Fig. 17: Effect of We_G and $\overline{q}$ on the drop diameter size of the spray

3.3.4.3 Drop size distribution along spray trajectory

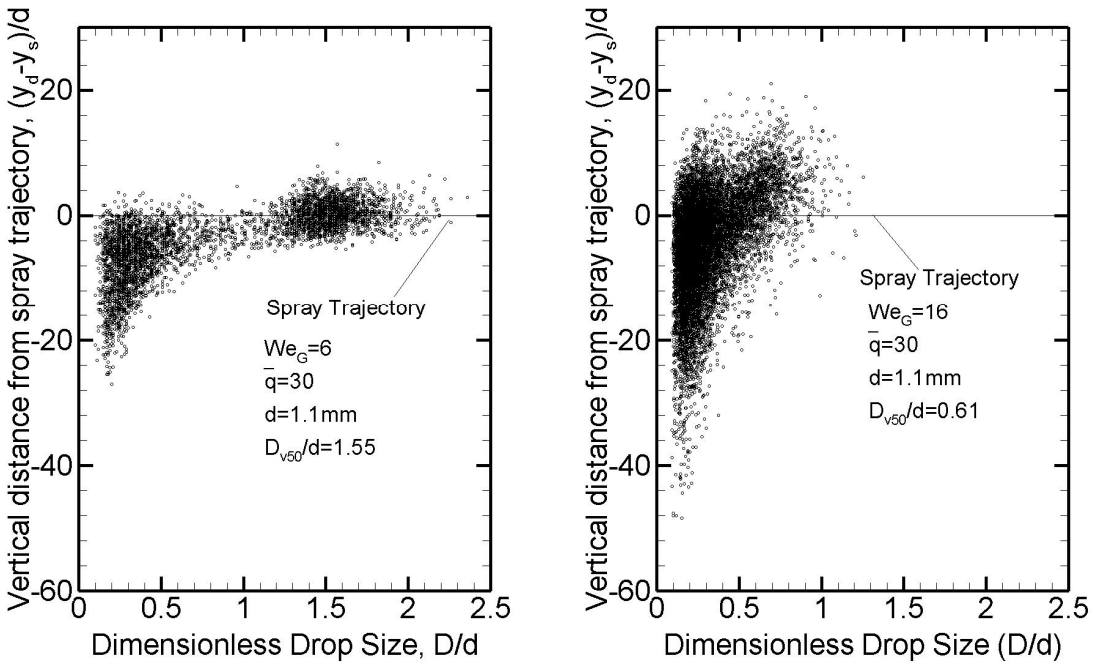

Fig.18: Drop size distribution along the spray trajectory

a) $We_G = 6$, $\bar{q} = 30$, $0.2 < We_d < 10.7$ b) $We_G = 8$, $\bar{q} = 30$, $0.05 < We_d < 30.0$

Drop size distribution along the spray trajectory of a jet both in column and bag breakup modes is provided in Fig. 18. The *y*-axis value is actually the relative vertical dimensionless distance between a droplet and the center of the spray along the spray trajectory as determined in previous section. The drop size range in the column breakup condition is around twice that of the bag breakup condition, with D_{v50}/d of 1.55 and 0.61 respectively. Dimensionless spray width is also different, with *W/d* of 30 and 60 for each case measured from the drop size distribution plot. There are more small droplets under the spray trajectory (the spray center based on mass flux), and the smaller the drops are, the further they are from the spray trajectory. The small drops have smaller *y*-component momentum and large surface/volume ratio hence larger drag force compared with big drops. They tend to follow the air flow and move away from the bulk spray. The big

drops, which determine the mass flux hence the spray trajectory, can stay in the upper region of the spray because of higher *y*-component momentum and lower drag force. The spray trajectory of the column breakup liquid jet is more compact, although there are small drops which still deviate from the main spray trajectory.

3.3.4.4 Mass flux along spray trajectory

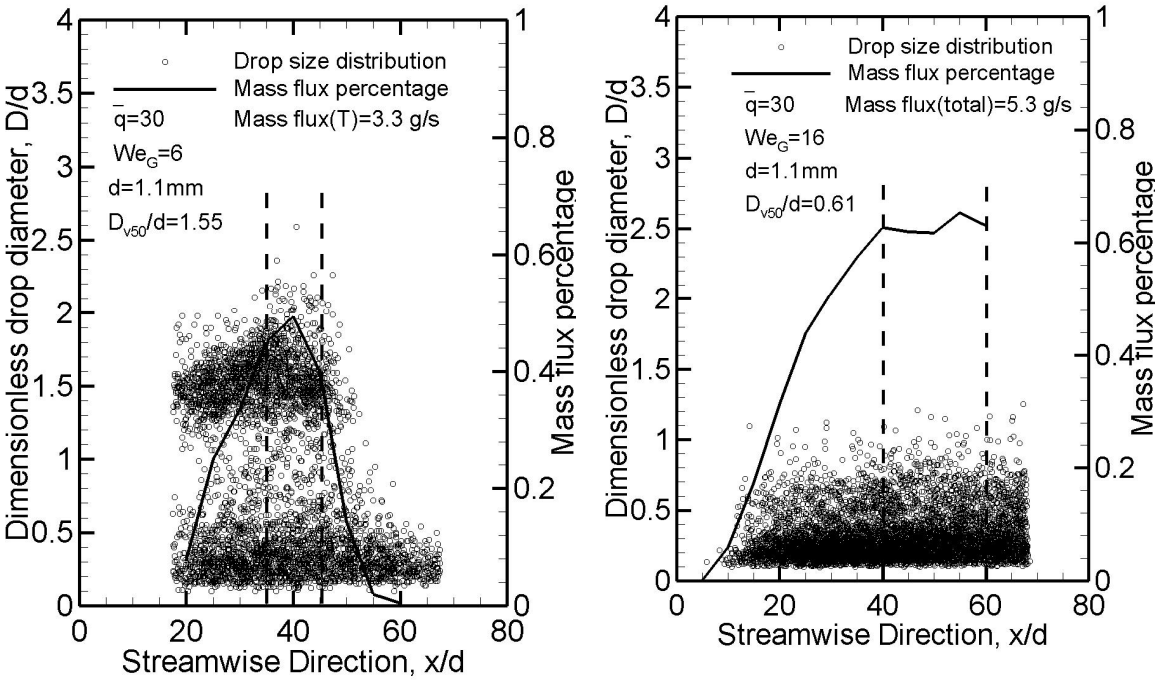

a) We_G = 6, 0.2 < We_d < 10.7, $\overline{q}$ = 30, Column breakup mode

b) We_G = 16, 0.05 < We_d < 30.0, $\overline{q}$ = 30, Bag breakup mode

Fig. 19: Drop size distribution and mass flux percentage of the spray respecting to streamwise direction.

Drop size distribution along the streamwise direction (*x/d*) and mass flux percentage are plotted in Fig. 19, with same momentum ratio and different gas Weber number. The whole field of view of the spray was divided into several slides with same width ($\Delta(x/d)=5$), and the mass flux percentage at location *x* was calculated as:

$$\frac{\dot{M}_x}{\dot{M}_T} = \frac{\sum_i (\rho_l V_d \frac{1}{6}\pi \cdot D^3)_i}{\rho_l V_j \pi (d/2)^2 \Delta x} = \frac{2}{3}\frac{\sum_i (V_d \cdot D^3)_i}{V_j d^2 \Delta x} \tag{12}$$

Here i means the i-th droplet in the region at *x* location.

As shown in the Fig. 19 b), mass flux percentage increases intensely in the early stage of the liquid jet (*x/d* < 40), and fluctuates around a certain value in the later stage. For this bag breakup case, the jet first breaks into bags and nodes which could not be recognized by the shadowgraph system resulting in low mass flux percentage. Then more droplets are formed from the breakup of bags and nodes, and also from the secondary breakup of fragments with big Weber number, which increases the captured mass flux. After *x/d* = 40, the mass flux percentage reaches 0.64 with small fluctuation, which indicates the completion of the secondary breakup. The post process software could not collect all of the flux for two reasons: fragments with non-circular shape could not be recognized as drops, some small drops are hard to match in two images hence no velocity obtained for them. At this stage, the spray can be considered to be fully developed. Similar with the mass flux percentage variation in Fig. 19 b), the percentage in Fig. 19 a) also increases in the early stage of the jet but does not reach the steady state. This is because the spray trajectory is out of the field of view when *x/d* reaches 40, so the camera only captured part of whole droplets. Since there is no secondary breakup in the first case as discussed in following section, it is reasonable to assume the column breakup in Fig. 19 a) is completed at *x/d* = 40.

Histograms of the droplets of the spray in steady stage are plotted in Fig. 20.

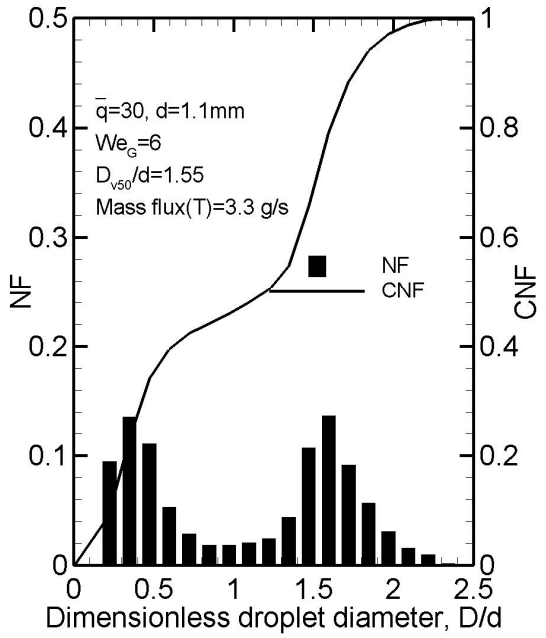

a) We_G = 6, 0.2 < We_d < 10.7

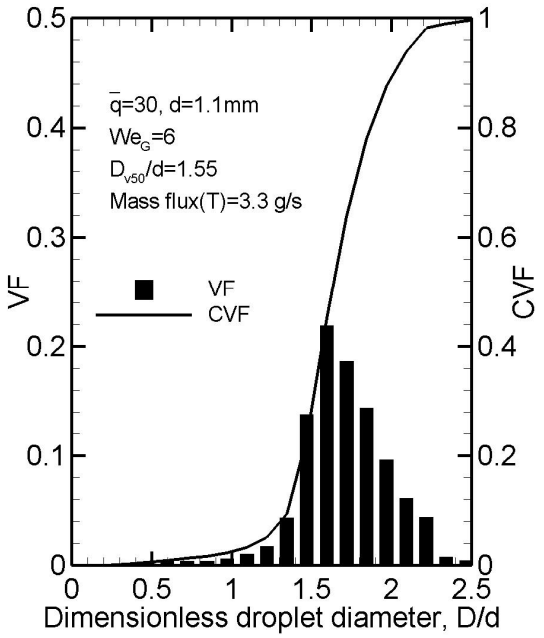

b) We_G = 6, 0.2 < We_d < 10.7

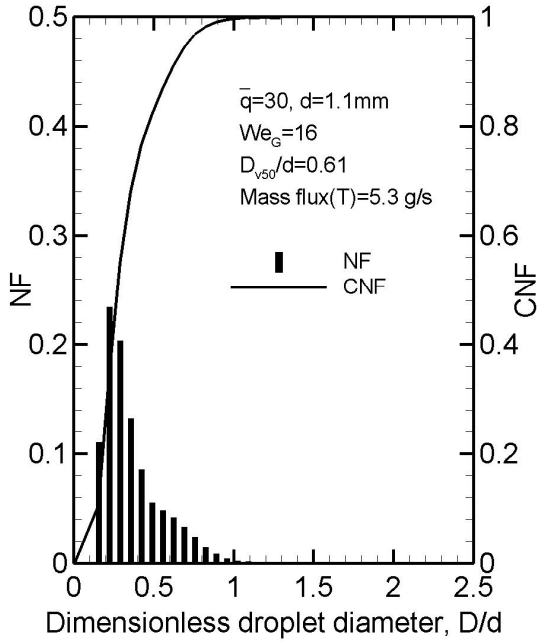

c) We_G = 16, 0.2 < We_d < 10.7

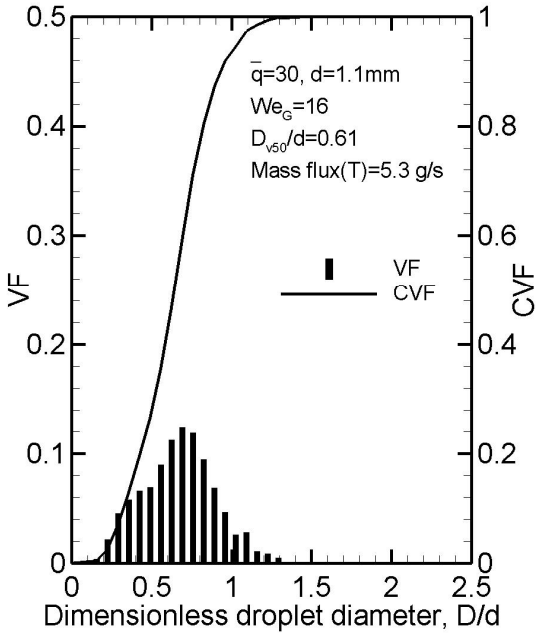

d) We_G = 16, 0.2 < We_d < 10.7

Fig. 20: Histogram of the spray, VF/CVF, NF/CNF

The number fraction of droplets in a) has a strong double peak distribution concentrating in two dimensionless size regions: size around 0.2 and 1.5, which is even larger than the initial jet diameter. Number fraction in c) with higher gas Weber number only focuses on one size range, which is below 1 and concentrates close on 0.2. There are two reasons which contribute to the difference of droplet size distribution for lower and higher We_G conditions, one is the primary breakup mode and the other is the secondary breakup after the column breakup. When the column breaks up, the liquid column breaks into ligaments and then into both large and small droplets, some droplets formed by ligaments have a diameter which is even larger than the initial jet diameter; these droplets do not have secondary breakup since their droplet Weber number are smaller than the critical value for a drop to breakup (We_{cri} =12 [26]) because of low relative velocity; For the second condition which is in bag breakup mode, the column breaks into bag shape structures whose membrane then breaks into smaller drops and rim breaks into comparatively lager drops which are all smaller than drops formed in a column breakup. Right after these drops are formed, those ones with high drop Weber number are 'split' by the air drag force and grow into smaller drops through secondary breakup.

Although there are two peaks of number fraction of droplet when We_G = 6, the large number of small drops do not affect the volume fraction of the spray as we can see in fig b). That's because the small drops are negligible compared with larger ones in volume since there is a big step between these two sizes. The volume fraction of the higher Weber number condition in Fig. 20 d) has two close peaks due to larger amount of small drops and absence of really large ones as appears in b).

3.3.4.5 Drop velocity distribution

To describe the drop velocity distribution in terms of drop diameter, a dimensionless velocity is introduced in this study as follows:

$$\overline{V} = \frac{u_d}{u_a} \tag{13}$$

Which describes how much the velocity of drops accelerates compared to the air velocity; Fig. 21 gives the dimensionless drop velocity distribution respecting to drop diameter for both column and bag breakup modes. For the column breakup case in a), big drops with dimensionless diameter *D/d* around 1.5 have u_d close to 0.1, while drops with *D/d* smaller than 0.5 have large range of $\overline{V}$ from 0 up to 0.68. This observation makes sense considering smaller drops have larger surface area/volume ratio, since they are accelerated more by the air drag forces. Drop size of the spray in the bag breakup mode is smaller, so the $\overline{V}$ can reach up to 0.84 as expected. The smaller drops in the second case are formed very soon after the liquid jet is injected from the nozzle, so they have more time in our field of view to accelerate than the drops in the first case even with same diameter.

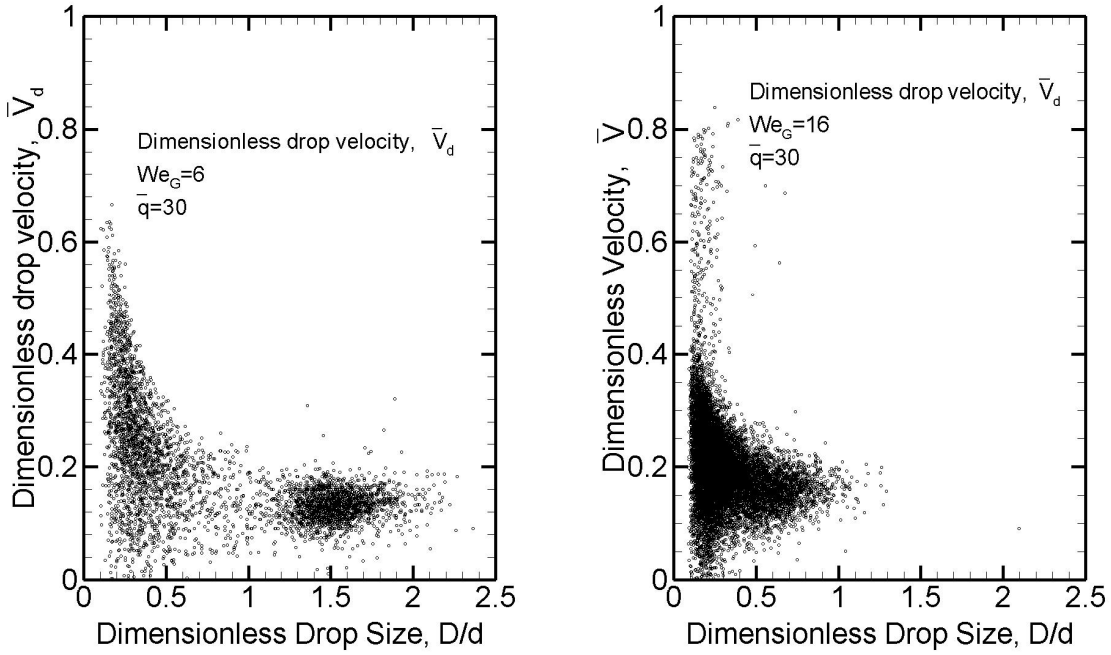

a) We_G = 6, $\bar{q}$ = 30, column breakup b) We_G = 16, $\bar{q}$ = 30, bag breakup

Fig. 21: Dimensionless drop velocity of the spray

Another dimensionless variable is $\bar{\theta}$, which is defined as follow:

$$\bar{\theta} = \frac{\theta_d - \theta_j}{\theta_a - \theta_j} \tag{14}$$

θ_d is the angle between the drop velocity and the streamwise direction *x*, $\theta_d = \arctan(\frac{v_d}{u_d})$

$\theta_j = \frac{\pi}{2}$, is the angle between the initial jet velocity and the streamwise direction *x*

$\theta_a = 0$, is the angle between the air velocity and the streamwise direction *x*

Dimensionless drop velocity angle for both column and bag breakup are shown in Fig. 22, which are similar with $\bar{V}$ because they are related with each other through drop velocity in cross-stream direction (*y*). Big drops have smaller velocity angle, which means they

are more tend to follow the liquid jet flow than smaller one. When the θ_d of smaller drops reaches up to 1, it means the v_d is smaller compared with u_d resulting in $\theta_d = 0$.

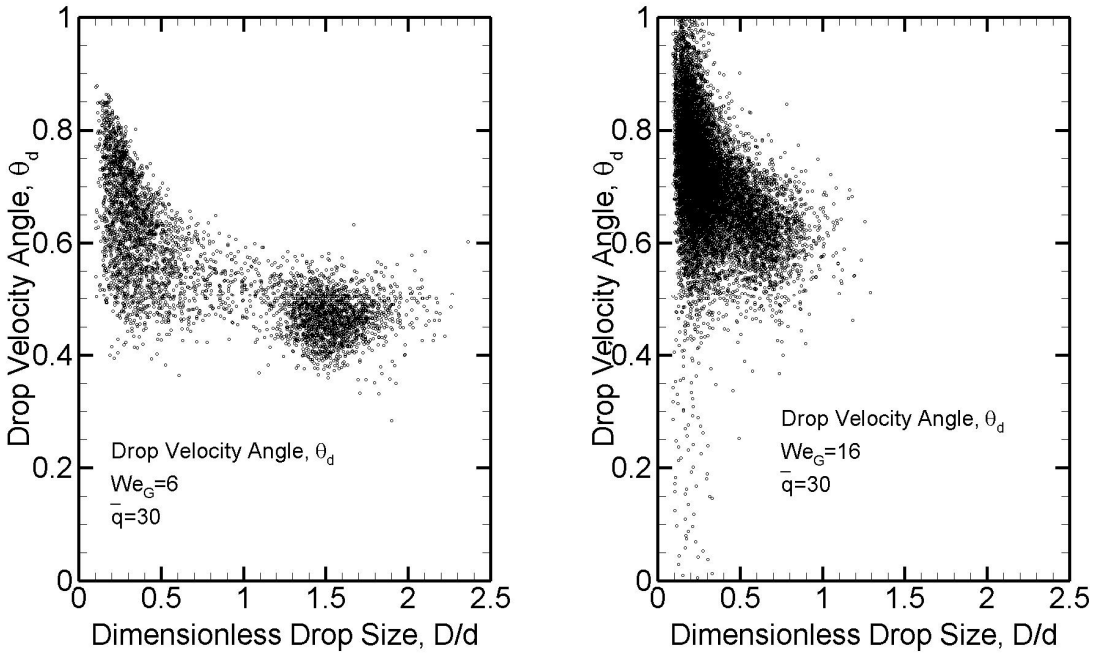

a) We_G = 6, $\overline{q}$ = 30, column breakup b) We_G = 16, $\overline{q}$ = 30, bag breakup

Fig. 22: Dimensionless drop velocity angle of the spray

4. Conclusion

An experimental study was conducted to investigate characteristics of the initial spray from a turbulent liquid jet in air crossflow. The experiment was conducted using water as the test liquid, an open circuit wind tunnel provided an uniform air velocity field as the crossflow. Shadowgraphy and Particle Image Velocimetry (PIV) techniques were used to capture trajectory of the column and spray, breakup locations, droplet size and velocity in the spray formed by column breakup and secondary breakup. Momentum ratio and gas Weber number were varied to study their effects on the characteristics of the jet both before and after breakup. The main results of this paper can be summarized as follows:

1) The jet column transverse is affected both by gas Weber number and momentum ratio, increasing We_G results in decreased column trajectory penetration (y_c) while increasing momentum ratio enhances the column trajectory penetration. A correlation is proposed to describe the effects of We_G and $\bar{q}$ on column trajectory:

$$\frac{y_c}{d} = 2.39\left(\frac{x_c}{d}\right)^{0.60} \bar{q}^{0.46} We_G^{-0.20}$$

$$0 < \frac{x_c}{d} < 20, \quad 10 < \bar{q} < 50, \quad 4 < We_G < 16$$

2) Consistent with previous study, column breakup location in the crossflow direction (x) is nearly constant over a range of experimental conditions. However, the breakup location is still affected by breakup mode. Two constants (depending on breakup regime- i.e. We_G) are provided:

$$\frac{x_b}{d} = \begin{cases} 5.9 & \mathrm{We_G} > 8 \\ 15.1 & \mathrm{We_G} \le 8 \end{cases}$$

3) Column breakup location in cross-stream direction (y) is governed by the momentum ratio. However, breakup distance is facilitied by large Weber number resulting in smaller y_b as described by:

$$\frac{y_b}{d} = \begin{cases} 10.7\bar{q}^{0.40} & \text{for } \mathrm{We_G} \le 8 \\ 4.46\bar{q}^{0.40} & \text{for } \mathrm{We_G} > 8 \end{cases}$$

4) Based on the measurements and observation in this study, the breakup regime boundary is redefined for bag breakup and column breakup, where the column breakup regime is given by a $We_G < 8$, transition regime is given by $8 < We_G < 12$ and bag breakup regime is given by $12 < We_G < 30$.

5) Spray trajectory (defined as the maximum mass flux line of the spray) is more sensitive to We_G and $\bar{q}$ than column trajectory, whose penetration increases with higher momentum ratio and low We_G. A correlation is provided for spray trajectory as:

$$\frac{y_s}{d} = 1.95\left(\frac{x_s}{d}\right)^{0.60} \bar{q}^{0.60} We_G^{-0.38}$$

$$10 < \frac{x_s}{d} < 100, \quad 10 < \bar{q} < 50, \quad 4 < We_G < 16$$

6) The gas Weber number We_G and momentum ratio affect the diameter of the spray in different ways, drop diameter keeps decreasing with increasing We_G while momentum ratio only affects drop size in the breakup transition regime ($8 < We_G < 12$).

7) Drop size distribution is different for lower and higher We_G, with larger D_{v50} and double peak concentrating center for lower We_G case. The reason why these large

drops can survive the whole spray is that their drop Weber number is smaller than a critical value, which means the secondary breakup would not happen.

8) Small drops have higher drop velocity in the same test condition, and they tend to follow the air crossflow resulting in dimensionless velocity angle close to 1. Big drops have relative lower drop velocity and their dimensionless velocity angles are smaller.

References

1. Wu, P.K., et al., *Breakup processes of liquid jets in subsonic crossflows.* Journal of Propulsion and Power, 1997. 13(1): p. 64-73.
2. Chen, T.H., et al. *Multi-zone behavior of transverse liquid jet in high-speed flow.* in *Proceedings of the 31st AIAA Aerospace Sciences Meeting and Exhibi*. 1993. Reno, NV, .
3. Iyogun, C.O., M. Birouk, and N. Popplewell, *Trajectory of water jet exposed to low subsonic cross-flow.* Atomization and Sprays, 2006. 16(8): p. 963-979.
4. Becker, J. and C. Hassa, *Breakup and atomization of a kerosene jet in crossflow at elevated pressure.* Atomization and Sprays, 2002. 12(1-3): p. 49-67.
5. Cavaliere, A., R. Ragucci, and C. Noviello. *Bending and break-up of a liquid jet in a high pressure airflow.* 2003: Elsevier Science Inc.
6. Stenzler, J.N., et al., *Penetration of liquid jets in a cross-flow.* Atomization and Sprays, 2006. 16(8): p. 887-906.
7. Bellofiore, A., A. Cavaliere, and R. Ragucci. *Air density effect on the atomization of liquid jets in crossflow.* 2007: Taylor & Francis Inc.
8. Ragucci, R., A. Bellofiore, and A. Cavaliere, *Trajectory and momentum coherence breakdown of a liquid jet in high-density air cross-flow.* Atomization and Sprays, 2007. 17(1): p. 47-70.
9. G. Vich and M. Ledoux, *Investigation of a Liquid Jet in a Subsonic Cross-Flow* Proc. ICLASS, 1997: p. 23-30.
10. Mazallon, J., Z. Dai, and G.M. Faeth, *Primary breakup of nonturbulent round liquid jets in gas crossflows.* Atomization and Sprays, 1999. 9(3): p. 291-311.

11. Sallam, K.A., C. Aalburg, and G.M. Faeth, *Breakup of round nonturbulent liquid jets in gaseous crossflow.* Aiaa Journal, 2004. 42(12): p. 2529-2540.

12. Birouk, M., B.J. Azzopardi, and T. Stabler, *Primary break-up of a viscous liquid jet in a cross airflow.* Particle & Particle Systems Characterization, 2003. 20(4): p. 283-289.

13. Birouk, M., T. Stabler, and B.J. Azzopardi, *An experimental study of liquid jets interacting with cross airflows.* Particle & Particle Systems Characterization, 2003. 20(1): p. 39-46.

14. O.A.Pulat, *Breakup of a Round Liquid Jet in a Low Weber Number Cross Flow.* 45th AIAA Aerospace Sciences Meeting and Exhibit, 2007. 8 - 11 January 2007, Reno, Nevada.

15. Inamura, T. and N. Nagai, *Spray characteristics of liquid jet traversing subsonic airstreams.* Journal of Propulsion and Power, 1997. 13(2): p. 250-256.

16. Wu, P.K., et al., *Spray structures of liquid jets atomized in subsonic crossflows.* Journal of Propulsion and Power, 1998. 14(2): p. 173-182.

17. Tambe, S., et al., *Liquid Jets in Subsonic Crossflow.* 43rd AIAA Aerospace Sciences Meeting and Exhibit, Reno, Nevada, Jan. 10-13, 2005.

18. Elshamy, O.M., *PIV and LDV Measurements for Liquid Jets in Crossflow* 45th AIAA Aerospace Sciences Meeting and Exhibit, 2007.

19. Ng, C.L., R. Sankarakrishnan, and K.A. Sallam, *Bag breakup of nonturbulent liquid jets in crossflow.* International Journal of Multiphase Flow, 2008. 34(3): p. 241-259.

20. White, F.M., *Fluid Mechanics, Sixth Edition.* 2008.

21. Raffel, M., C. Willert, and J. Kompenhans, *Particle Image Velocimetry.* Ist edition, Springer-Verlag, 1998.

22. Aalburg, C., et al., *Properties of nonturbulent round liquid jets in uniform gaseous cross flows.* Atomization and Sprays, 2005. 15(3): p. 271-294.

23. Chou, W.H. and G.M. Faeth, *Temporal properties of secondary drop breakup in the bag breakup regime.* International Journal of Multiphase Flow, 1998. 24(6): p. 889-912.

24. Abramowitz, M. and I.A. Stegun, *Handbook of Mathematical Functions with Formulas, Graphs, and Mathematical Tables.* 1965.

25. Fuller, R.P., et al. *Effects of injection angle on atomization of liquid jets in transverse airflow.* 2000: Amer Inst Aeronaut Astronaut.

26. Pilch, M. and C.A. Erdman, *Use of Breakup Time Data and Velocity History Data to Predict the Maximum Size of Stable Fragments for Acceleration-Induced Breakup of a Liquid-Drop.* International Journal of Multiphase Flow, 1987. 13(6): p. 741-757.